LARGE-SCALE STRUCTURE OF THE ATMOSPHERE OF THE QUIET SUN, CORONAL HOLES, AND PLAGES AS DEDUCED BY TOMOGRAPHY STUDY

V. M. BOGOD and A. S. GREBINSKIJ
Special Astrophysical Observatory RAS, Karachaevo – Cherkessia, Nizhnij Arkhyz 357147, Russia

(Received 7 August 1996; accepted 13 May 1997)

Abstract. We present here the results of emission tomography studies, based on a new differential deconvolution method (DDM) of Laplace transform inversion, which we use for reconstruction of the coronal emission measure distributions in the quiet Sun, coronal holes and plage areas. Two methods are explored. The first method is based on the deconvolution of radioemission brightness spectra in a wide wavelength range (1 mm – 100 cm) for temperature profile reconstructions from the corona to the deeper chromosphere. The second method uses radio brightness measurements in the cm – dm range to give a coronal column emission measure (EM).

Our results are based on RATAN-600 observations in the range 2.0 – 32 cm supplemented by the data of other observatories during the period near minimum solar activity. This study gives results that agree with known estimates of the coronal EM values, but reveals the absence of any measurable quantities of EM in the transition temperature region $3 \times 10^4 – 10^5$ K for all studied large-scale structures. The chromospheric temperature structure ($T_e = 20\,000 – 5800$ K) is quite similar for all objects with extremely low-temperature gradients at deep layers.

Some refraction effects were detected in the decimeter range for all types of large-scale structures, which suggests the presence of dense and compact loops (up to $N_e = (1–3) \times 10^9$ cm^{-3} number density) for the quiet-Sun coronal regions with temperature $T_e > 5 \times 10^5$ K.

1. Introduction

As is known from X-ray solar observations, large-scale coronal structures are a conglomerate of loops at a variety of scales. Results of reconstruction for the same object may be quite diverse in optical and radio waves because of the great differences in opacities. For a true physical picture of the solar structures, combined multi-wavelength imaging observations (Aschwanden, 1995) are required.

Such combined studies have revealed two related problems: a deficiency of observed solar radio brightness (Chambe, 1978) compared to that expected from EUV measurements (Raymond and Doyle, 1981) of differential emission measure (DEM) and the ambiguous nature of corona–chromosphere transition region (CCTR) structure (Dere, 1982; Feldman, 1983). All attempts to smooth out the first problem by EUV recalibrations (see Zirin, Baumert, and Hurford, 1991 for review) had failed. New radio brightness calibrations (see Grebinskij, 1987, Zirin, Baumert, and Hurford, 1991) only deepened the problem and led these authors to the conclusion that a clue to its solution lay in the total absence of CCTR in the observed radioemission. This position agrees with Feldman's conclusions: EUV observations (Feldman and Laming, 1994) suggest that there is no stratified CCTR for the quiet Sun as a whole, nor for individual flux tubes.

Solar Physics **176:** 67–86, 1997.
© 1997 *Kluwer Academic Publishers. Printed in Belgium.*

In this paper we attempt to shed light on these problems for large-scale solar structures (quiet Sun, mean coronal holes, plages) using the deconvolution of free–free brightness temperature spectra. This approach, known as emissive tomography in medicine (Natterer, 1990) or image-spectroscopy in astronomy (Piddington, 1954; Bogod and Grebinskij, 1994; Gary and Hurford, 1994), leads to direct estimation of the DEM distribution along the line of sight without any suppositions. Together with stereoscopic techniques for estimating the heights and shapes of active regions (Aschwanden and Bastian, 1994), it gives information independent of that from optical and X-ray studies.

We present here a new, efficient deconvolution technique (differential deconvolution method (DDM)) based on the Laplace transform, and give some reconstruction results for the emission measure (EM) and temperature distribution in large-scale coronal structures. Our results confirm Feldman's statements about CCTR. Also we have found clear observational signatures for the presence of a strong refraction effect, which leads to a direct measurement of coronal electron density fluctuations.

2. Differential Deconvolution Method (DDM)

We present here a new deconvolution technique based on the integral transform

$$f(p) = \int_0^\infty y(t) e^{-t/p} \, \mathrm{d}t/p \, , \tag{1}$$

and use it to reconstruct solar atmospheric structures by deconvolution of brightness temperature spectra $T_b(\lambda)$ from radio observations. The brightness temperature is described by the radiation transfer equation in the Rayleigh–Jeans approximation, as

$$T_b(\lambda) = \int_0^{\tau_{\max}} T_e(l) e^{-\tau} \, \mathrm{d}\tau. \tag{2}$$

Here the optical thickness $\tau(l, \lambda)$ is a function of depth l along a line of sight, which for the case of free-free emission can be written

$$\mathrm{d}\tau = \lambda^2 \, \mathrm{d}t, \quad \mathrm{d}t = 2 \times 10^{-22} N_e^2 T_e^{-3/2} \, \mathrm{d}l \, , \tag{3}$$

where t is a normalized radio depth $t(l) = \tau(l, \lambda = 1 \text{ cm})$. After substitution of an inverse function $l = l(t)$ as an argument of $T_e(l)$ and introducing the definition $p = \lambda^{-2}$, one gets from (2) the equation

$$T_b(p) = \int_0^{t_{\max}/p} T_e(t) e^{-t/p} dt/p \, . \tag{4}$$

For any sufficiently optically thick astrophysical plasma, $t_{\max}/p \gg 1$ and (4) approaches the desired form (1). After solving the deconvolution problem for transform (4) we can calculate a differential emission measure DEM(T_e) of the emission source from its definition (Raymond and Doyle, 1981)

$$\mathrm{DEM}(T) = \int\limits_{0.891T}^{1.122T} N_e^2 \,\mathrm{d}l = 1.1 \times 10^{21} T^{5/2} \frac{\mathrm{d}t(T)}{\mathrm{d}T} \ , \tag{5}$$

where $t = t(T)$ is an inversion of reconstructed $T_e(t)$ distribution. After some suppositions relating N_e to T_e (e.g. constant pressure or heat flux), one can reconstruct the spatial distributions of $N_e(l)$ and $T_e(l)$ by integrating Equation (3) as

$$\mathrm{d}T_e/\mathrm{d}l = k' N_e^2(T_e) T_e^{-3/2} / (\mathrm{d}t(T_e)/\mathrm{d}T_e) \ .$$

It is instructive to represent Equation (1) as a smoothing transform at logarithmic coordinate scales as

$$x = \log t, \quad s = \log p, \quad f(p) \to \Phi(s), \quad y(t) \to Y(x) \ , \tag{6}$$

$$\Phi(s) = \int\limits_{-\infty}^{\infty} H(s-x) Y(x) \,\mathrm{d}x, \quad H(s) = e^{Ms - e^{Ms}} \ , \tag{7}$$

where $M = Ln(10)$. From the plot of the kernel function $H(s)$ (see Figure A1(a)) one can find a relatively large effective width $W_H = 1.0$ at 0.5 level.

Many inversion methods for the Laplace transform in the form

$$g(\varepsilon) = \int\limits_{0}^{\infty} y(t) e^{-\varepsilon t} \,\mathrm{d}t/\varepsilon \tag{8}$$

have been developed (see Piana, Brown, and Thompson, 1995 for review). We wish to note that the form given in equation (1) is also equivalent to this form by substitutions $p = 1/\varepsilon, f(p) = p^{-2}$, and $g(\varepsilon = p^{-1})$. Thus, the literature cited by Piana, Brown, and Thompson (1995) is relevant to this work also.

The basic idea of DDM differs from traditional algebraic approaches. We describe it with a simple example (Grebinskij, 1985). Let $y(t)$ be a power function in Equation (1). Then we have from (1)

$$y(t) = a\, t^n, \quad f(p) = \Gamma(1+n) a\, p^n \ , \tag{9}$$

where $a, n > -1$ are the free parameters, $\Gamma(x)$ – Euler gamma function. The problem of deconvolution is to find the unknown $y(t)$ using the known $f(p)$. To solve this problem we make use of exact equations in the case of power functions

(9) of Equation (1). To achieve this goal we have to differentiate Equation (9) for $f(p)$ with respect to its argument p according to the number of free parameters. For example, after one differentiation one can obtain all free parameters through values of $f(p)$ and its derivative:

$$n = \frac{pf^{'}(p)}{f(p)}, \; a = \frac{f(p)}{p^n \Gamma(1+n)} \; . \tag{10}$$

The next step is to substitute these expressions for n and a into Equation (9) for $y(t)$. Now we can introduce a differential reconstruction operator $G(p)$,

$$G(p) = \frac{1}{\Gamma(1 + pf'(p)/f(p))} \; . \tag{11}$$

Changing the variables $y(t = p) = y(p)$, we can express the solution through the reconstruction operator $G(p)$:

$$y(t = p) = G(p)f(p) \; . \tag{12}$$

This is a fundamental definition for the Differential Deconvolution Method (DDM). For the family of trial functions (Equation (9)) we have an exact solution of the deconvolution problem with the reconstruction operator $G = 1/\Gamma(1 + n)$. The functional relation (12) is valid for all possible values of free parameters, so there is no need to find out their real values for a given distribution of $f(p)$. This is the main difference with algebraic approaches, where we need to expand with a polynomial or a series approximation for $y(p)$, and different approximations may give quite different results (see Chambe, 1978). We may stress this point further by another example for a family of trial functions as an infinite power series

$$y(t) = a_0 + a_1 t + a_2 t^2 + a_3 t^3 + \cdots \; , \tag{13}$$

with an exact reconstruction operator G as

$$G(p) = 1 - \frac{1}{4}\frac{p^2 f^{''}}{f} + \frac{1}{9}\frac{p^3 f^{'''}}{f} - \cdots \; . \tag{14}$$

There is a deep difference between these trial functions: the first (9) is a fully adaptive one, but the other (13) is a rigid (fixed powers) and so much less effective in reconstruction problems.

2.1. Practical realization

For practical implementations we use a higher-order trial function

$$T_e(t) = a_1 t^{n_1} + a_2 t^{n_2} + a_3 t^{n_3} \; , \tag{15}$$

with 6 free parameters. For that case the exact reconstruction operator is

$$G(p) = 1 + b_1 p^1 \frac{T_b'}{T_b} + b_2 p^2 \frac{T_b''}{T_b} + b_3 p^3 \frac{T_b'''}{T_b} \; . \tag{16}$$

We would treat the three parameters n_i ($i = 1, 2, 3$) as the known ones (see below). In that case the unknown coefficients b_i ($i = 1, 2, 3$) in Equation (16) are independent from parameters a_i of (15) and are determined by solution of the linear equation system

$$n_i b_1 + n_i(n_i - 1) b_2 + n_i(n_i - 1)(n_i - 2) b_3 = \frac{1}{\Gamma(1 + n_i)} - 1 \; . \tag{17}$$

To optimize the deconvolution algorithm, one should choose appropriate values for parameters n_i ($i = 1, 2, 3$). As is seen from Equation (7), the inversion problem is localized by the finite width of the kernel function: the bulk of the information about $Y(x)$ at point $x = x_0$ is obtained from $\Phi(s = x_0 \pm W/2)$. For the 6-parameter trial function family one can use as primary information the values of the measured function $\Phi(s)$ and its derivatives at three points of argument s: one at the centre and two on the borders of the region of influence: $s_0 = \log t_0, s_\pm = s_0 \pm W/2$. To achieve a full adaptivity, we chose indexes n_i as spectral indexes $n(p)$ of $T_b(p)$ at the mentioned values of $s = \log p$. For details of the numerical code see Appendix.

2.2. DDM RESOLUTION ESTIMATES

For Equation (7) we can use image-restoration criteria (see, for example, Frieden, 1975). We take $Y(x)$ as an 'original-source' function, and the restored function $\tilde{Y}(x) = G\Phi(s = x)$ as an 'image'. The two are related by

$$\tilde{Y}(s) = \int_{-\infty}^{\infty} \mathrm{PSF}(s - x) Y(x) \, \mathrm{d}x \; , \tag{18}$$

where the point spread function (PSF) is an image of an original $Y(x)$ as a δ-function. Resolution of DDM is described by an effective width W_{PSF} of the smoothing kernel PSF and its sidelobe level. There is a straightforward way to calculate a PSF. For point source $y_0 = t_0 \delta(t - t_0)$ in Equation (1) one gets the response $f_0 = (t_0/p) \exp(-t_0/p)$. After its deconvolution, one gets an image $\tilde{y}(t_0, t) = G f_0$, which after a change to logarithmic scales (6) becomes a PSF. A plot of this PSF(s) for the adopted numerical DDM code (see Appendix) is shown in Figure A1(a) as $H(s)$ plot. From these plots note that the PSF effective width, $W_{\mathrm{PSF}} = 0.5$ is much less than for the primary $H(s)$ smoothing kernel. A low sidelobe level without any oscillations leads to great dynamic range of the reconstructed images. There is some asymmetry of the PSF shape and a small systematic displacement $\log(s_{\max}) - \log(x_0) = 0.15$.

The results of numerical simulations for the several step-wise model distributions of $T_e(t)$ are presented in Figures A1(b–d). The parameters of these 4-layer simulations are chosen to match some expected properties of real atmospheric brightness $T_b(p)$ (see below).

2.3. DDM STABILITY ESTIMATES

To achieve a stable inversion for real problems with a noisy observed $f(p)$ distribution one should filter the primary data after changing them to double logarithmic scales: $f(p) \to F(s)$, where $F = \log(f)$ as discussed in the Appendix. A random noise r.m.s. level increases after deconvolution proportionally to spatial frequencies $K_F = 2\pi/\Lambda$ of disturbances because of the growth of the spectral index $n = \mathrm{d}F/\mathrm{d}x$ (for example, $n = \Lambda a \cos(\Lambda x)$ for $\delta\Phi = a \sin(\Lambda x)$) and the great nonlinearity of reconstruction operator G (see a case of $G = 1/\Gamma(1+n)$ as an example). The solution disturbances grow infinitely for $\Lambda \to 0$, but filtration of $F(s)$ (in double logarithmic scales) at spatial scales $\Lambda < W_{\mathrm{PSF}}$ would guarantee restoration stability without changing its resolution.

3. Coronal Emission Measure Estimation by the Spectral Index Deconvolution (SID) Method

We describe now the case when the observed radiation is the sum of optically thin but hot and optically thick but cold layers. For this case there is an efficient way to separate the parameters of the hot layer regardless of the presence and parameters of cold. For the two-layer model chromosphere–corona with 3 parameters $(T_{\mathrm{chr}}, T_c, t_c)$ and the brightness spectrum

$$T_b(p) = T_c(1 - e^{-t_c/p}) + e^{-t_c/p} T_{\mathrm{chr}} \ , \tag{19}$$

one can get the exact solution for the coronal layer. After double differentiation of both sides of the equation with respect to p, we have

$$t_c = p(1 + n + m) \ , \tag{20}$$

$$T_c = \frac{T_b(p)(1+m)}{(1+n+m)} \ , \tag{21}$$

$$\langle t_c \, T_c \rangle = (1+m) p T_b(p) \ , \tag{22}$$

where we introduced the first and second logarithmic derivatives of $T_b(p)$

$$n = n(p) = p\frac{T_b'(p)}{T_b(p)}, \quad m = m(p) = p\frac{n'(p)}{n(p)} \ . \tag{23}$$

Here the coronal parameter $\langle t_c\, T_c \rangle$ is the column emission measure of the coronal layer weighted by $T_c^{0.5}$:

$$\mathrm{EM}(T_c) = N_e^2\, L_c = 5 \times 10^{21}\, \langle t_c\, T_c \rangle\, T_c^{0.5}\ . \tag{24}$$

That estimate does not depend on wavelength range and may be used for coronal EM calculations based on coronal brightness $T_b(\lambda)$ measurements at centimetric–decimetric wavelengths, where the emission is not dominated by refraction effects (contrary to meter-wave measurements). The temperature weighting function of estimate (24) is quite different from that given by X-ray measurements, and therefore gives an independent source of information on the EM of solar corona relative to X-rays.

4. Observational Data

The deconvolution methods developed above were put into practice to reconstruct various structures of the solar atmosphere (quiet-Sun center, coronal holes and plages) using data from the RATAN-600 in the wavelength range 2–32 cm. For improvement of the calibration accuracy of quiet-Sun measurements, the OVRO observations from Zirin, Baumert, and Hurford (1991) were as well. Where available, data from other instruments in a wider range (1 mm–3 m) were used also.

4.1. Quiet-Sun disk center

Here we use the RATAN 600 spectral measurements of the quiet Sun made during the minimum phase of the solar activity cycle. The results of observations at 9 wavelengths (in the range of 1.8–31.6 cm) with one-dimensional resolution $20''$–$300''$ were summarized by Borovik (1994), and OVRO measurements at 20 frequencies for the same range were presented by Zirin, Baumert, and Hurford (1991).

In the short wavelength part of the spectrum ($\lambda < 1$ cm) we have used the results of fan-beam observations in the 1–9 mm band (Fedoseev and Chernishev, 1988), which are well approximated by linear regression as $T_b(\lambda) = 5160 + 400\lambda\,[\mathrm{mm}] \pm 200$ K.

In the longer wavelength part of the spectrum ($\lambda > 30$ cm) there are no multiwave measurements made with a single instrument, which is why we use estimations obtained with different instruments at various wavelengths made during the minimum of solar activity (see Table I).

4.2. Coronal holes

Our coronal hole study is based on the spectral data obtained through the cooperative efforts of several observatories in the range 1–300 cm, which were compiled

Table I
Meter–decimeter radiobrightness

λ [cm]	T_b [10^3 K]	Reference
73.5	550	(Trottet and Lantos, 1978)
74.3	630	(Chiuderi-Drago, Avignon, and Thomas, 1977)
90	600	(Sheridan and McLean, 1985)
178	1150	(Trottet and Lantos, 1978)
247	1200	(Kundu, Gergely, and Erickson, 1977)
375	1000	(Dulk and Sheridan, 1974)
407	820	(Kundu, Gergely, and Erickson, 1977)
1140	470	(Kundu, Gergely, and Erickson, 1977)

by Papagiannis and Baker (1982). These estimates are consistent with RATAN-600 one-dimensional observations (Borovik *et al.*, 1990).

4.3. Plage area

An excessive brightness of plage area in the active region AR 3804 was measured at 7 wavelengths (2–21 cm band) during VLA–RATAN-600 cooperative observations (15 July 1982) by subtraction of the local source contributions to one-dimensional radio scans (Akhmedov *et al.*, 1987). These results are in agreement with short-wave (up to $\lambda = 1$ cm) brightness measurements, compiled by Urpo, Hildebrandt, and Krüger (1987) and are consistent with early studies using the RATAN-600 observations (Bogod and Gelfreikh, 1980).

4.4. Data reduction

All observational data for each wavelength were transformed to a function of parameter $p = \lambda\ [\text{cm}]^{-2}$ and smoothed in a double logarithmic scale $\log(T_b) - \log(p)$ by cubic spline regression (see Appendix for details). Final results are presented in Table II with step $\mathrm{d}\log(p) = 0.1$ in the range $\log(p) = -5.0$–2.1 (wavelengths 300 cm–1 mm) for the quiet-Sun center, coronal holes, and plage areas.

5. Tomography Reconstruction Results

We describe here the results of tomography studies of the quiet Sun, coronal holes, and plage using both deconvolution methods on the data of Table II.

5.1. Differential deconvolution method

5.1.1. *Quiet-Sun Disk Center*

In Figures 1(a–d) we present the $T_e(t)$ reconstruction results by the DDM for the quiet-Sun center based on the brightness temperature spectrum $T_b(p)$ in the broad

Table II
Observed radio brightness (smoothed)

$\log(p)$	f, GHz	$\log(T_b)$ Sun	Hole	Plage	$\log(p)$	f, GHz	$\log(T_b)$ Sun	Hole	Plage
−5.0	0.095	6.017			−1.4	5.98	4.183	4.122	4.475
−4.9	0.106	6.033			−1.3	6.71	4.155	4.100	4.411
−4.8	0.119	6.044			−1.2	7.53	4.129	4.080	4.351
−4.7	0.134	6.049			−1.1	8.45	4.105	4.062	4.296
−4.6	0.150	6.046	5.974		−1.0	9.48	4.085	4.046	4.247
−4.5	0.168	6.036	5.944		−0.9	10.64	4.061	4.031	
−4.4	0.189	6.018	5.908		−0.8	11.94	4.043	4.017	
−4.3	0.212	5.993	5.868		−0.7	13.40	4.026	4.004	
−4.2	0.238	5.961	5.824		−0.6	15.03	4.010	3.990	
−4.1	0.267	5.922	5.774		−0.5	16.87	3.994	3.977	
−4.0	0.300	5.877	5.718		−0.4	18.92	3.978	3.964	
−3.9	0.336	5.827	5.655		−0.3	21.23	3.962	3.950	
−3.8	0.377	5.770	5.583		−0.2	23.82	3.946	3.937	
−3.7	0.423	5.707	5.504		−0.1	26.73	3.932	3.925	
−3.6	0.475	5.637	5.419		0	30.00	3.917	3.912	
−3.5	0.533	5.561	5.329		0.1	33.66	3.903	3.900	
−3.4	0.598	5.480	5.235		0.2	37.76	3.890	3.888	
−3.3	0.671	5.396	5.139		0.3	42.37	3.876	3.875	
−3.2	0.753	5.310	5.043		0.4	47.54	3.863	3.863	
−3.1	0.845	5.223	4.948		0.5	53.34	3.851	3.851	
−3.0	0.948	5.135	4.857		0.6	59.85	3.840	3.840	
−2.9	1.06	5.049	4.771		0.7	67.16	3.829	3.830	
−2.8	1.19	4.965	4.692		0.8	75.35	3.821	3.820	
−2.7	1.34	4.884	4.621		0.9	84.55	3.813	3.813	
−2.6	1.50	4.807	4.556	5.509	1.0	94.86	3.806	3.806	
−2.5	1.68	4.732	4.499	5.411	1.1	106	3.800	3.800	
−2.4	1.89	4.661	4.447	5.312	1.2	119	3.794	3.794	
−2.3	2.12	4.592	4.399	5.216	1.3	134	3.789	3.789	
−2.2	2.38	4.528	4.356	5.121	1.4	150	3.784	3.784	
−2.1	2.67	4.469	4.317	5.029	1.5	168	3.778	3.778	
−2.0	3.00	4.414	4.281	4.940	1.6	189	3.773	3.773	
−1.9	3.36	4.366	4.249	4.855	1.7	212	3.767	3.767	
−1.8	3.77	4.322	4.220	4.770	1.8	238	3.761	3.761	
−1.7	4.23	4.282	4.193	4.691	1.9	267	3.754		
−1.6	4.75	4.246	4.168	4.615	2.0	300	3.746		
−1.5	5.33	4.213	4.144	4.543	2.1	336	3.736		

range of wavelengths. The electron temperature $T_e(t)$ distribution in the radio depth range $\log(t) = -4.5$–1.8 for different layers from corona to deep chromosphere is presented. Because of the great dynamic range of the electron temperatures, these results are shown separately in Figures 1(a) and 1(b) for the corona and chromosphere with different temperature scales.

Our chromospheric reconstruction results (see Figure 1(b)) represent the first attempt to obtain direct information about temperature structure $T_e(t)$ by its own radioemission in the deepest chromospheric layers up to radio depths $t = 100$ (normalized to wavelength 1 cm) and electron temperatures up to $T_e(t) = 5800$ K. As can be seen, the low chromosphere is highly isothermal with two slight but distinctive temperature plateaus: one at $T_e = 7500$ K (radio depth about $t = 1$) and another at $T_e = 5900$ K (radio depth about $t = 10$).

In the CCTR the reconstruction shows (see Figure 1(a)) a step-wise drop from coronal to chromospheric temperatures. The validity of this picture may be evaluated by taking into account the error spread of observed spectra (see Figure 1(d)). It presents quiet-Sun T_b multifrequency measurements obtained by using two different instruments (Zirin, Baumert, and Hurford, 1991; Borovik, 1994). These results are so close, that we have to amplify their dispersion by use of the equalization factor $p^{-0.5}$). The discrepancy is less then 2% at $\log(p) > -1$ at centimeter wavelengths and grows in the decimeter range with systematic and random errors up to 10%. One can construct slightly different smoothed spectra $T_b(p)$ within the error bars using slightly different hardness of spline regression. Results of such calculations are shown in Figure 1(a) for four variants of smoothing: hardness factor 0.97 (lowest curve, minimum smoothing), 0.96 (adopted values in Table II), 0.95 and 0.94 (maximum smoothing). Each of these spectra was deconvolved and the results are presented also in Figure 1(a). As is seen, our deconvolution results are weakly sensitive to the observational errors for chromospheric layers (in the region with $\log(t) > -3$), but in the CCTR the deconvolution results become unstable without additional smoothing. As is seen from Figure 1(a), the degree of difference $\log(G) = \log(T_b(p = t)) - \log(T_e(t))$ is rather small at coronal and chromospheric levels ($\log(G) < 0.5$), but becomes extremely high (up to $\log(G) = 1.5$) in the CCTR.

From the data shown in Figure 1(a) one can evaluate the radio depth in the CCTR where the temperature changes from chromospheric ($\log(T_e) < 4.3$) to coronal ($\log(T_e) > 5.5$) values. This value is extremely low: $\log(t_c) = -3.5 \pm 0.1$. Because the deconvolution procedure leads to smoothing of step-wise $T_e(t)$ distributions with the displacement about $\mathrm{d}\log(t) = -0.6$ (see Figure 1(c)), we can evaluate the real coronal opacity as about $\log(t_c) = -4.1$.

In the region of coronal layers we can use spectral data $T_b(p)$ with minimal smoothing (see Figure 2(b)) which reveal the existence of the bend point on reconstructed $T_e(t)$ profiles at $\log(T_e) = 5.7$. This may be interpreted as evidence of two distinctive coronal structures with the temperatures T_e above 1.5×10^6 K for one and 5×10^5 K for the other.

In the upper chromosphere, the $T_e(t)$ temperature profile is not monotonic. There are two temperature maxima: first ($\log(T_e) = 4.3$ at $\log(t) = -2.8$) and a second ($\log(T_e) = 4.2$ at $\log(t) = -1.9$). In Figure 1(c) we present the deconvolution

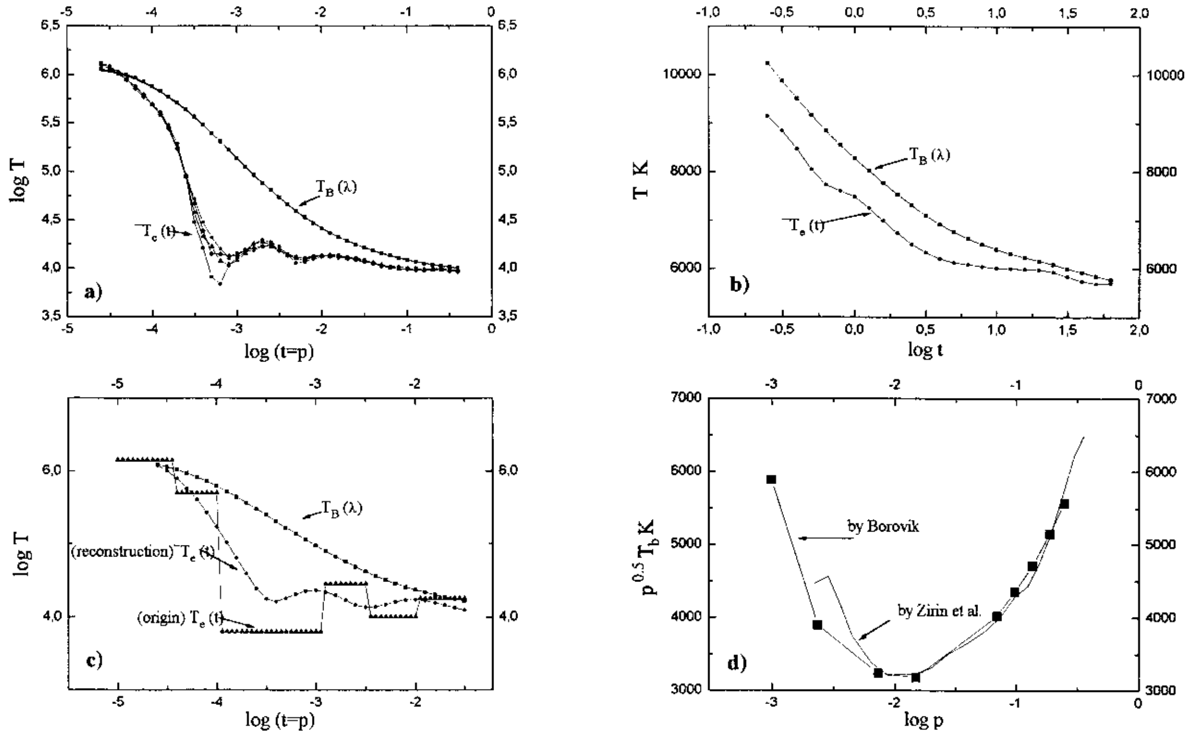

Figure 1. Deconvolution results for the quiet-Sun brightness spectrum. (a) A family of deconvolved electron temperature $\tilde{T}_e(t)$ profiles as a function of normalised radio depth $t = \tau(\lambda = 1 \text{ cm})$ for the same observed brightness spectrum $T_b(p = \lambda^{-2})$ for four variants of its smoothing. (b) Electron temperature $\tilde{T}_e(t)$ reconstruction results for the deep chromosphere by cm−mm wavelength brightness spectrum $T_b(\lambda)$ deconvolution. (c) A simulated step-wise $T_e(t)$ model distribution to match reconstruction results in (a). We show three curves: (1) a model original $T_e(t)$ distribution, (2) its brightness spectrum $T_b(\lambda)$, and (3) a restored $^{\sim}T_e(t)$ by $T_b(\lambda)$ spectrum deconvolution. A comparison of this reconstruction with the results for observed spectra deconvolution (a) shows the possibility of detection of non-monotonic $T_e(t)$ distributions by a DDM techniques. (d) A comparison of two quiet-Sun center brightness spectra observed from the two different observatories. Both of the spectra were normalised by the multiplication factor $p^{0.5}$ to enhance the dispersion. The systematic deviations in decimetric wavelengths ($\log(p) < -2$) are due to the different calibration approaches: a uniform brightness disc (Zirin, Baumert, and Hurford, 1991) and near limb brightness enhancement by Borovik (1994).

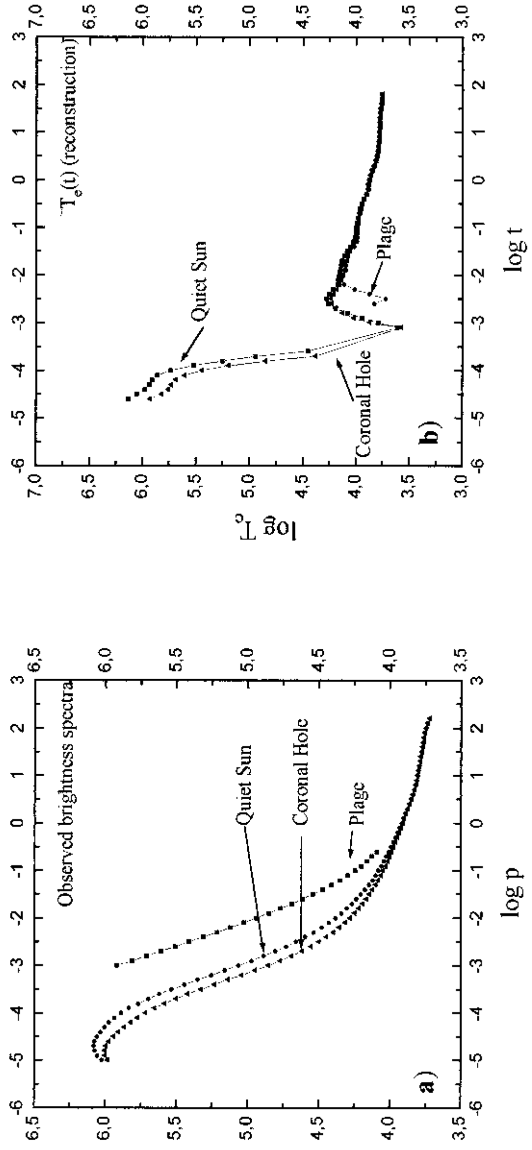

Figure 2. Electron temperature $T_e(t)$ profile reconstruction for the quiet Sun, coronal holes, and plage areas by deconvolution of an unsmoothed brightness spectra $T_b(\lambda)$. (a) The observed brightness spectra $T_b(p)$ with a minimum of additional smoothing. (b) The restored electron temperature $\tilde{T}_e(t)$ profiles.

model based on a step-wise approximation of the tomography results above with a cool layer between the corona and the chromosphere. These results confirm the possibility of obtaining diagnostics of nonmonotonic temperature structures.

5.1.2. *Coronal Holes and Plages*

In Figure 2 we present tomography $T_e(t)$ reconstruction results for coronal holes, plages and quiet Sun for direct comparison of atmospheric structure in these objects. Brightness temperature spectra $T_b(p)$ and $T_e(t)$ of these objects are presented in Figure 2(a) and 2(b) respectively. As is seen, the deconvolution reveals a great similarity of the atmosphere for all objects at chromospheric temperatures ($T_e < 10^{4.3}K$): the $T_e(t)$ distributions coincide within deconvolution accuracy (see Figure 2(b)). So the major differences appear to lie in the coronal temperature layers.

5.2. Spectral index deconvolution

In Figures 3(a) and 3(b) we show the calculated values of the coronal parameter $< t_c T_c >$, defined in Section 4, for the quiet Sun, coronal hole, and plage area using the spectral index method (SID).

As was shown above, this approach is a good one for two-component (corona and chromosphere) temperature $T_e(t)$ reconstructions. In that case, calculations by expression (22) would give the same results (24) for $\mathrm{EM_c}$ at any frequency. This precondition is fulfilled in the real solar atmosphere (see above), so the method is applicable. We have used here the brightness temperature spectra in the frequency range ($\log(p) = -3.5$–2.0, where the first deconvolution method has lead to unstable $T_e(t)$ reconstruction results. The SID method gives quite stable estimates of $\langle t_c T_c \rangle$ for all objects, and these values have only a weak dependence on frequency (see Figure 3(b)) despite rather strong spectral index $n(p)$ variations (see Figure 3(a)).

The calculated values of $\langle t_c\ T_c \rangle$ show that the coronal emission measure is greatly enhanced in plages ($\langle t_c\ T_c \rangle = 790$ as compared to the quiet Sun ($\langle t_c\ T_c \rangle = 110$) and is significantly diminished in coronal holes ($\langle t_c\ T_c \rangle = 60$), see Figure 3(b)). This directly confirms the conclusion that most of the observed brightness $T_b(p)$ enhancement in plage areas and the corresponding depression in coronal holes (see Figure 2(a)) is due to coronal emission variations.

For mean coronal temperatures of about $T_c = 1.5 \times 10^6$ K, we find coronal radio depths through $\langle t_c T_c \rangle$ as $\log(t_c) = -4.2$, -4.45, and -3.3 for quiet-Sun center, coronal hole and plage respectively. Column emission measure may be evaluated by Equation (24). For quiet-Sun center we have $N_e^2 L_c = 4.1 \times 10^{26}$ cm^{-5}, in good agreement with the value EM $= (3.7 \pm 0.5) \times 10^{26}$ cm^{-5} from the brightness distribution across the solar disk (see Lantos, 1979, for a review). The direct $\langle t_c \rangle$ estimation by deconvolution of the metric brightness spectra (see above) gives essentially the same values of coronal radio depth. This is a rather unexpected

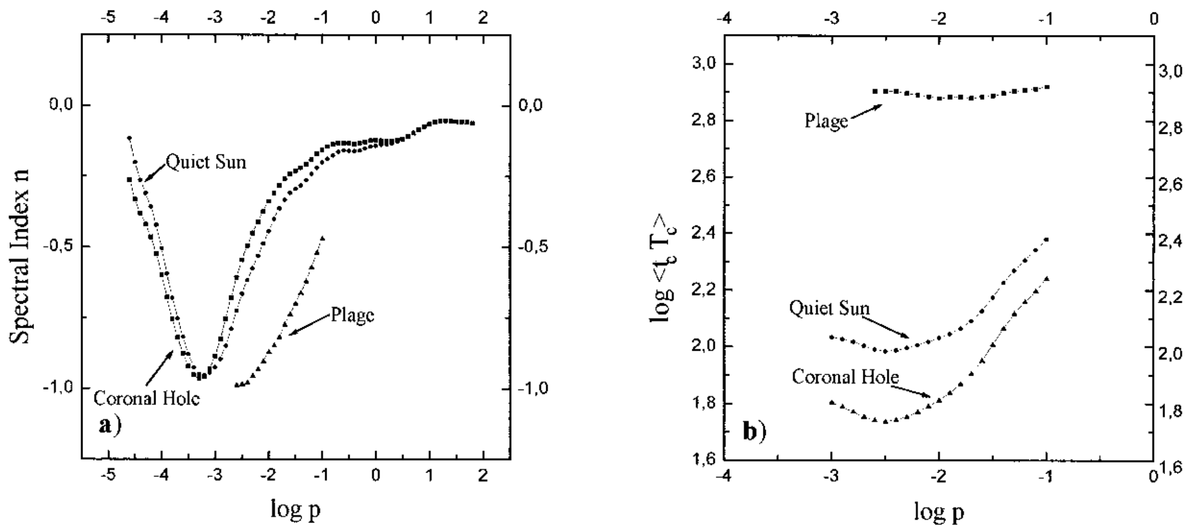

Figure 3. Results of the coronal parameter $\langle t_c T_c \rangle$ evaluations by the spectral index method for the quiet Sun, coronal holes and plage areas. (a) The spectral indexes $n(p) = \mathrm{d}\log(T_b)/\mathrm{d}\log(p)$ for observed brightness spectra $T_b(p)$ in Figure 2(a). (b) The coronal parameter $\langle t_c\ T_c \rangle$ values estimates for different wavelengths in the cm$-$dm range.

result because the possible refraction and reflection phenomena in the solar corona should be quite different at metric and decimetric wavelengths.

6. Discussion

Tomography is a sensitive tool for discovery of the most subtle details of the solar atmosphere, which are totally masked in the usual spectral research. Our study shows that the reconstructed temperature distribution consists practically of two layers with chromospheric and coronal temperatures without intermediate ones. This was also known before, but only for the quiet Sun (Grebinskij, 1987; Zirin, Baumert, and Hurford, 1991). Now we suggest the same behaviour for structures with quite different magnetic field topology (closed fields for plages, open for coronal holes). As was stressed in these papers this indicates the presence of extremely compact and closely spaced fine-scale loop structures in the CCTR.

Another important result is the deep temperature depression between the chromosphere and corona, discovered for all of the reconstructed $T_e(t)$ profiles. This may be a real manifestation of the presence of cold matter, as deduced from some EUV observations (see Schmahl and Orrall, 1979; Pneuman and Kopp, 1978), but here we have an alternative suggestion.

For a full explanation of the observed brightness temperature spectra one should take into account refraction effects. Refraction phenomena in free–free radiation transfer may be introduced through the refractive index $N_{\text{ref}}(\nu) = (1 - \nu_L^2/\nu^2)$ in opacity (Zheleznyakov, 1970)

$$d\tau(p) = dt/p \rightarrow dt/pn(p),\ n^2(p) = 1 - P_{cr}/p\ , \tag{25}$$

where $P_{cr} = 10^{-13} N_e$.

Refraction effects lead to two opposite influences on the brightness temperature T_b: (a) decrease of T_b at low frequences ($p < P_{cr}$) due to displacement of the reflection point to a height in the atmosphere above where $\tau = 1$, and (b) increase of T_b at the higher frequences $p \geq P_{cr}$ near the local point of reflection (where the index of refraction $n < 1$).

The second effect also leads to an increase in the slope ($\mathrm{d}\log T_b/\mathrm{d}\log p$) of the spectrum in a relatively narrow band (where $n \rightarrow 0$) near the local plasma frequency. We show the importance of refraction for the deconvolution in a simple manner by introducing refraction in the second coronal layer of our trial model (see Figure 1(c)) as

$$T_{b\ \text{cor}}(p) = \begin{cases} T_1(1 - exp(-2t_1/p)), & p < P_{cr} \\ T_1(1 - exp(-t_1/p)) + T_2(1 - exp(-t_2/p\, n(p))), & p > P_{cr}\ . \end{cases} \tag{26}$$

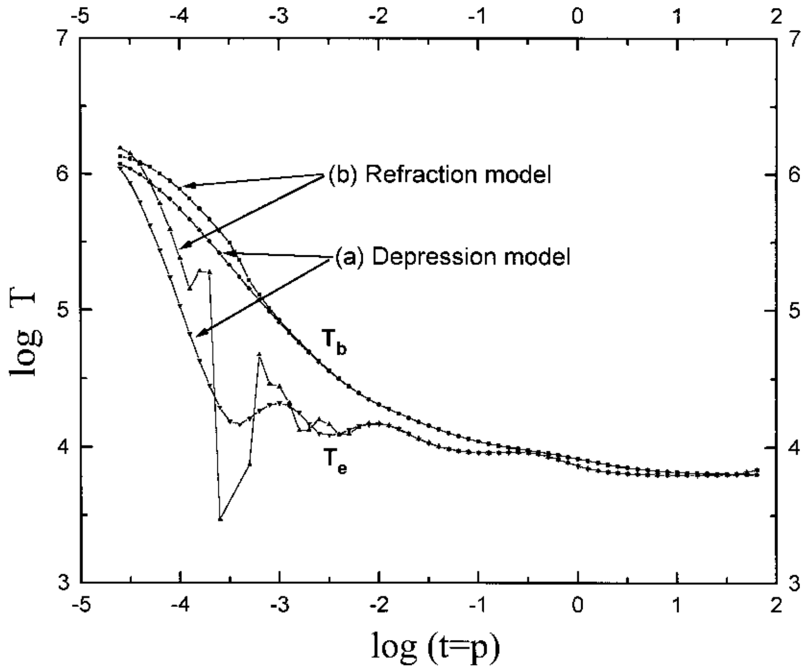

Figure 4. Refraction effects simulations. All observed brightness spectra $T_b(p = \lambda^{-2})$ mentioned have an extremely high spectral index values $n_{\min}(p) = -0.95$–0.98, close to a breaking point $n = -1$ in the decimetric wavelengths. There are two possible causes of this: a refraction effects in the dense coronal loops or a deep temperature depression between chromosphere and corona. The DDM reconstruction technique takes no account of the refraction and so leads to a fictitious temperature minimum up to a full deconvolution break. We illustrate this with $\tilde{T}_e(t)$ reconstruction results of two simulated brightness spectra $T_b(p)$: the first one (a) for a model with a deep temperature minimum at CCTR without refraction in the coronal layer, and the other one (b) with refraction effects in corona but without a temperature minimum. In both cases the deconvolution of the simulated $T_b(p)$ breaks in the CCTR temperature range, as it takes place for unsmoothed observed spectra (see Figure 2). We treat this break as an observational signature of the presence of refraction effects in the coronal radioemission.

Here, for simplicity, we have neglected the reduction of effective opacity t_1 at low frequencies. For a value of the free parameter P_{cr} in our calculations, we adopted $P_{cr} = p_{\min}$, where $p_{\min}$ is the minimum point of the spectral index $n(p)$ curve (see Figure 3(a)). At that frequency range the enhancement of the brightness spectrum slope due to refraction becomes greatest, because the steepest change of opacity occurs at $n = (1 - P_{cr}/p) \to 0$. For observed quiet-Sun brightness spectra we find $\log(p_{\min}) = -3.5$, so we assume $P_{cr} = 10^{-3.5}$ in Equation (26) to match the observations. The model brightness spectrum $T_b(p)$ and its deconvolution $T_e(t)$ are shown in Figure 4 for two cases: (a) refraction trial model without a chromosphere-corona depression and (b) with depression but without refraction. As expected, the inclusion of refraction solves the main problems: the $T_b(p)$ spectrum with refraction effects becomes steeper at $p \ll P_{\min}$ and the deconvolved $T_e(t)$ distribution has a deep minimum in the transition zone. Such simplified estimates confirm the importance of taking into account refraction and scattering effects in the inner corona as well as in the outer corona (see Bastian, 1992, for a review).

Comparison of observations with models including refraction effects may lead to the possibility of directly measuring the characteristic number density through the relation $N_e = 10^{13} P_{cr}$. Our preliminary estimation $N_e = (1–3) \times 10^9$ cm^{-3} may suggest the existence of high-density plasma in coronal regions, associated with coronal loops. However, we will need much more sophisticated refraction models before achieving a quantitative treatment of these problems.

Acknowledgements

The authors are indebted to M. Aschwanden and G. Gelfreikh for suggestions after reading the manuscript. We thank the referee, D. Gary, for his constructive comments. This program of research has been partially supported by the Russian Foundation for Basic Research (RFBR) Projects 96−02−16598a and 96−02−16268a. Also, the work had a partial support of INTAS grant 94−4625.

Appendix. DDM Numerical Code

The primary spectral data are a set of measured values of brightness T_b at discrete wavelengths λ_i: $T_{bi} = T_b(\lambda_i)$. A numerical deconvolution code includes three steps.

(I) DATA REDUCTION

The practical restoration operator $G(p)$, (16)–(17), includes only the logarithmic derivatives. For data with a large dynamical range we should transform all data to a double logarithmic scale after changing arguments λ to $p = \lambda$ [cm]$^{-2}$: $F_i = \log T_b(\lambda_i)$ and $x_i = -2\log(\lambda_i)$.

Next, we fit some continuous function $F(x)$ by a cubic spline least-squares technique for unequally spaced data and then digitize it by step $\delta x = 0.1$ as F_k. The data set thus obtained is smoothed again by a 7-point moving cubic least-square filter. Double smoothing with unequal and then equal spacings guarantees that short-term disturbances are removed, while derivatives up to third order are unchanged.

(II) CALCULATION OF DERIVATIVES

All derivatives in definition (16) of restoration operator G should be calculated with maximum accuracy and stability. We use definitions:

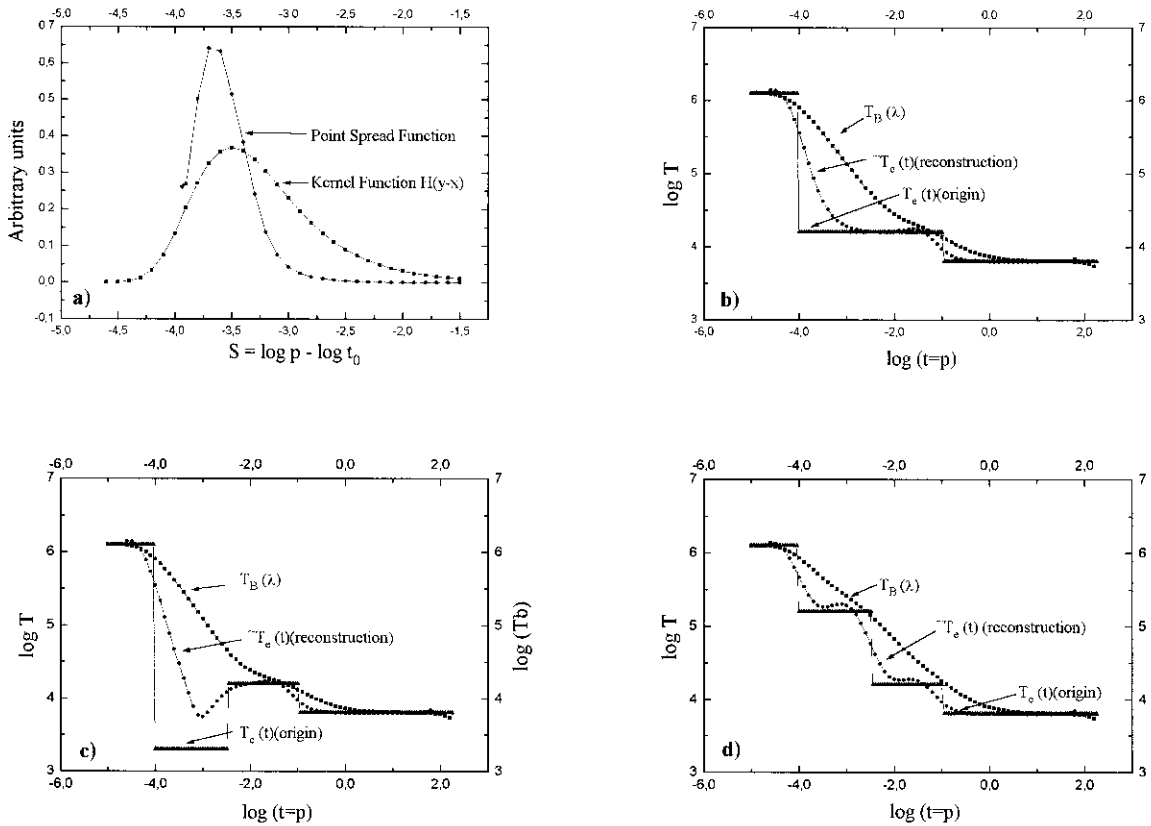

Figure A1. (a) Plots of smoothing kernels on logarithmic scales: $H(s)$, for an original transform (7), and $PSF(s)$, for a point spread function (18) with $\log(t_0) = -3.5$ after a DDM reconstruction. An effective PSF(s) width is half as wide with respect to $H(s)$. (b–d) Restoration of electron temperature $\tilde{T}_e(t)$ profiles by brightness spectra $T_b(p)$ family (28) deconvolution for different original step-wise $T_e(t)$ electron temperature distributions.

$$pf'/f = A, \qquad p^2f''/f = A(A-1) + B/M \ ,$$

$$p^3f'''/f = A(A^2 - 3A + 2) + 3B(A-1)/M + C/M \ ,$$

where $M = Ln(10)$ and $A = \mathrm{d}F/\mathrm{d}x, B = \mathrm{d}^2F/\mathrm{d}x^2, C = \mathrm{d}^3F/\mathrm{d}x^3$ are calculated on the same 5-point grid with step $h = 0.2$ by an enhanced accuracy code:

$$A(x_k) = (F_{k-2} - 8F_{k-1} + 8F_{k+1} - F_{k+2})/(12h) \ ,$$

$$B(x_k) = (-F_{k-2} + 16F_{k-1} - 30F_k + 16F_{k+1} - F_{k+2})/(12h^2) \ ,$$

$$C(x_k) = (-F_{k-2} + 2F_{k-1} - 2F_{k+1} + F_{k+2})/(2h^3) \ .$$

The combination of an extended grid interval and a high accuracy code gives both accuracy and stability of derivatives.

INDEXES AND FINAL SOLUTION

For the simplest estimation of spectral indexes $n_i = dF_i/dx$ we take values at three regions of the same 5-points grid as

$$n_2 = A, \quad n_1 = (F_{k-1} - F_{k-2})/h, \quad n_3 = (F_{k+2} - F_{k+1})/h \ . \tag{27}$$

For $1/\Gamma(1+n)$ we take a polynomial expansion $1/\Gamma(x) = x(1+x)(1+a_1x + \cdots + a_8x^8)$ for $x = [-1, 1]$ and use the definition $\Gamma(1+x) = x\Gamma(x)$ for extension to any x. After solving Equations (17) for b_k, the inversion is completed by calculation of G through (16) and final restoration of $y(t)$ at the point $\log(t) = x_k$ as $Y_k = y(x_k)$ by definition (12): $\log(Y_k) = \log(G) + F_k$. The adopted code guarantees the smoothness of $f(p)$ and its derivatives up to third order and smoothness of the solution $y(t)$ up to its first order derivative.

As examples of reconstruction results, we show in Figures A1(b) and A1(c) some numerical simulations for the model distribution

$$f(p) = T_1(1 - e^{-t_1/p}) + e^{-t_1/p}T_2(1 - e^{-t_2/p}) + e^{-(t_1+t_2)/p}T_3(1 - e^{-t_3/p}) + T_4 \tag{28}$$

with $T_1 = 10^{6.15}, T_3 = 10^{4.2}, T_4 = 10^{3.7}$ and $t_1 = 10^{-4}, t_2 = 10^{-2.5}, t_3 = 10^{-1}$. We undertake a reconstruction for three different values of parameters $T_2 = 10^{4.2}$ (see figure A1(b)), $T_2 = 10^{3.3}$ (see figure A1(c)) and $T_2 = 10^{5.2}$ (see figure A1(c)). On each figure we show plots of the original $y(t)$, the resulting observable spectrum $f(p)$ and the restored $\tilde{y}(t = p)$. We can interpret $f(p)$ (28) as the radio brightness $T_b(p)$ of an atmosphere with a step-wise $y(t) = T_e(t)$ electron temperature distribution for the parameters mentioned. From comparison of original and restored $T_e(t)$ distributions one can see acceptable restoration results by DDM technique without significant oscillations for the quite different source functions.

References

Akhmedov, Sh. B., Bogod, V. M., Borovik, V. N., Willson, R. F., Gelfreikh, G. B., Dikij, V. N., Korjavin, A. N., Lang, K. R., and Petrov, Z. E.: 1987, *Izv. SAO* **25**, 105.
Aschwanden, M. J.: 1995, *Lecture Notes in Physics* **444**, 13.
Aschwanden, M. J. and Bastian, T. S.: 1994, *Astrophys. J.* **426**, 425.
Bastian, T. S.: 1994, *Astrophys. J.* **426**, 774.
Bogod, V. M. and Gelfreikh, G. B.: 1980, *Solar Phys.* **67**, 29.
Bogod, V. M., Grebinskij, A. S., and Opeikina, L. V.: 1994, *CESRA Workshop on Coronal Magnetic Energy Releases*, Caputh, Germany, May 16–20, 1994, p. 46.
Bogod, V. M., Vatrushin, S. M., Abramov-Maximov, V. E., Tsvetkov, S. V., and Dikij, V. N.: 1993, *ASP Conference Series* **46**, 306.
Borovik, V. N.: 1994, *Lecture Notes in Physics* ,**432**, 185.
Borovik, V. N., Kurbanov, M. Sh., Livshitz, M. A., and Ryabov, B. I.: 1990, *Astron. Zh.* **67**, 1038.
Chambe, G.: 1978, *Astron. Astrophys.* **70**, 255.
Chiuderi-Drago, F., Avignon, Y., and Thomas, R. J.:1977, *Solar Phys.* **51**, 143.
Dere, K. P.: 1982, *Solar Phys.* **75**, 189.
Dulk, G. A. and Sheridan, K. V.: 1974, *Solar Phys.* **36**, 191.
Fedoseev, L. I. and Chernishev, V. I.: 1988, in 'XX Vsesouynaja konferentsyia po radiofizicheskim issledovaniym solnechnoi sistemi', Tezisi dokladov, Poselok Nauchnij, oktjabr 1988, Simferopolj, p. 12.
Feldman, U.: 1983, *Astrophys. J.* **275**, 367.
Feldman, U. and Laming, J. M.: 1994, *Astrophys. J.* **434**, 370.
Frieden, B. R.: 1975, in T. S. Huang (ed.), *Picture Processing and Digital Filtering*, Springer-Verlag, Springer, p. 105.
Gary, D. E. and Zirin, H.: 1990, *Astrophys. J.* **355**, 321.
Gary, D. E. and Hurford, G. J.: 1994, *Astrophys. J.* **420**, 903.
Grebinskij, A. S.: 1985, *Astron. Zh.* **62**, 768.
Grebinskij, A. S.: 1987, *Soviet Astron. Letters* **13**, 4.
Kundu, M. R., Gergely, T. E., and Erickson, W. C.: 1977, *Solar Phys.* **53**, 489.
Lantos, P.: 1978, *Astron. Astrophys.* **62**, 69.
Natterer, F.: 1986, *The Mathematics of Computerized Tomography*, Wiley and Sons, New York.
Papagianis, M. D. and Baker, K. B.: 1982, *Solar Phys.* **79**, 365.
Piana, M., Brown, J. C., and Thompson A. M.: 1995, *Solar Phys.* **156**, 315.
Piddington, J. H.: 1954, *Astrophys. J.* **119**, 531.
Pneuman, G. W. and Kopp, R. A.: 1978, *Solar Phys.* **57**, 49.
Raymond, J. C. and Doyle, J. G.: 1981, *Astrophys. J.* **247**, 686.
Schmahl, E. J. and Orrall, F. Q.: 1979, *Astrophys. J.* **231**, L41.
Sheridan, K. V. and McLean, D. J.: 1985, in D. J. McLean and N. R. Labrum (eds), *Solar Radiophysics*, Cambridge University Press, New York, p. 443.
Trottet, G. and Lantos, P.: 1978, *Astron. Astrophys.* **70**, 245.
Urpo, S., Hildebrandt, J., and Krüger, A.: 1987, *Solar Phys.* **112**, 119.
Zheleznyakov, V. V.: 1970, *Radio Emission of the Sun and Planets*, Pergamon Press, New York.
Zirin, H., Baumert, B. M., and Hurford, G. J.: 1991, *Astrophys. J.* **370**, 779.